Bulgarian Chemical Communications, Volume 58, Issue 2 (pp. 136-142) 2026 DOI: 10.34049/bcc.58.2.5726

Zn-doped $SrBi_2O_4$ nanopowders prepared by sol-gel method and their photocatalytic properties

H. N. E. Rabiaa[1], H. Benhebal[1*], O. Sebbah[2], S. Kadi[3], S. Lellou[3], A. Farcy[4], J. G. Mahy[4], S. D. Lambert[4]

[1]*Department of Chemistry, Faculty of Matter Sciences, University of Tiaret, Tiaret 14000, Algeria*
[2]*Synthesis and Catalysis Laboratory, University of Tiaret, Tiaret 14000, Algeria*
[3]*Biodiversity, Health and Valorization of Biological Resources Laboratory, Department of Biology, University of Tiaret, Tiaret 14000, Algeria*
[4]*Department of Chemical Engineering–Nanomaterials, Catalysis and Electrochemistry, B6a, University of Liège, 4000 Liège, Belgium*

Received: October 18, 2025; Revised: February 07, 2026

The aim of this work is to synthesize photocatalysts usable in the decomposition processes of organic pollutants under visible irradiation. In this context, pure and zinc-doped $SrBi_2O_4$ spinel oxide powders were synthesized by sol-gel process. Physical and chemical properties of the calcination nanoproducts were characterized by XRD, FTIR spectroscopy, BET surface area and SEM. Congo red was selected as a model dye to evaluate the photocatalytic activity of the materials. The formation of spinel structure was confirmed by XRD and infrared spectroscopy. The nanometric size of the crystallites undergoes a decrease following the incorporation of zinc ions. On the other hand, all powders display very low specific surfaces between 0.1429 and 0.3549 m^2/g. Low zinc doping in this case (1-3%) was favorable to boost the activity of $SrBi_2O_4$ which gave an 84% degradation of the dye after 3 hours of irradiation.

Keywords: $SrBi_2O_4$, doping, sol-gel, photocatalysis, Congo red

INTRODUCTION

Water, a precious natural resource, is without competition the essence of life, so meeting human needs for drinking water has become one of the main concerns around the world. However, many countries are now facing an imminent drinking water supply crisis due to excessive consumption and high contamination of surface water [1]. Wastewater loaded with toxic molecules such as dyes constitutes one of the main sources of water pollution [2]. Due to the diversity and complexity of dye structures, most physical, biological and chemical treatments used for water purification remain ineffective and are limited only to the transfer of contamination from one phase to another [3]. Oxidation reactions of organic pollutants by heterogeneous photocatalysis carried out in aqueous media with dispersions of inorganic photocatalysts under light irradiation have widely become an effective approach for water treatment [4]. However, the application of photocatalytic processes is primarily conditioned by the choice of the material used as a photocatalyst. While some semiconductors such as titanium dioxide, zinc oxide and others have been widely studied, their use has been limited only to ultraviolet radiation, which further reduces the profitability of such treatment. Following the efforts deployed in the field of nanotechnology, new photocatalysts sensitive to visible light have emerged. Among these materials there are spinel oxides of structure AB_2O_4 of which A and B are metal cations of valences +2 and +3, respectively [5, 6]. Bismuth-based spinels MBi_2O_4 have recently received great attention as promising candidates for the removal of organic pollutants by visible light photocatalysis due to their low band gap energies [7, 8]. Only a few reports have been published on the use of $SrBi_2O_4$ as a photocatalyst under visible light for the photodegradation of dyes. According to Shtarev and Serpone's review [9], only three works have been devoted to the study of the $SrBi_2O_4$ system [10-12]. The objective of the present study is to develop pure and zinc-doped $SrBi_2O_4$ nanoparticles and to evaluate their photocatalytic activity for the degradation of dyes in aqueous solution. The sol-gel method was used for the synthesis of pure and Zn-doped $SrBi_2O_4$ photocatalysts. Physical and chemical properties of the calcined nanoproducts were characterized by X-ray diffraction (XRD), Fourier transform infrared spectroscopy (FTIR), specific surface area measurement (BET), and scanning electron microscopy (SEM). Congo red (CR) was chosen as a model dye to evaluate the photocatalytic activity of the materials.

---

* To whom all correspondence should be sent:
Email: *benhebal@univ-tiaret.dz*

EXPERIMENTAL

Materials

Strontium nitrate [$Sr(NO_3)_2$], bismuth nitrate pentahydrate [$Bi(NO_3)_3.5H_2O$], zinc nitrate tetrahydrate [$Zn(NO_3)_2.4H_2O$] and citric acid $C_6H_8O_7$ were used as starting materials without prior treatment.

- *Synthesis of Zn-doped $SrBi_2O_4$ photocatalysts.* Zn-doped $SrBi_2O_4$ photocatalysts were synthesized by a facile sol–gel citrate method (Fig. 1). Distilled water was used as solvent throughout all synthesis steps. The stoichiometric amounts of strontium nitrate and bismuth nitrate pentahydrate at a molar ratio of 1:2 were dissolved in distilled water. To this mixture, citric acid solution was added. The pH was adjusted by ammonium hydroxide solution. The solution was stirred and then the appropriate amount of zinc nitrate (1, 3 and 5 wt %) was added to the mixture, followed by vigorous stirring at 80 °C. The obtained dry gels were further ground and calcined at 600 °C for 4 h. The as-synthesized products with various Zn contents (0, 1, 3 and 5 wt%) were labelled as SB, ZSB(1%), ZSB(3%) and ZSB(5%), respectively.

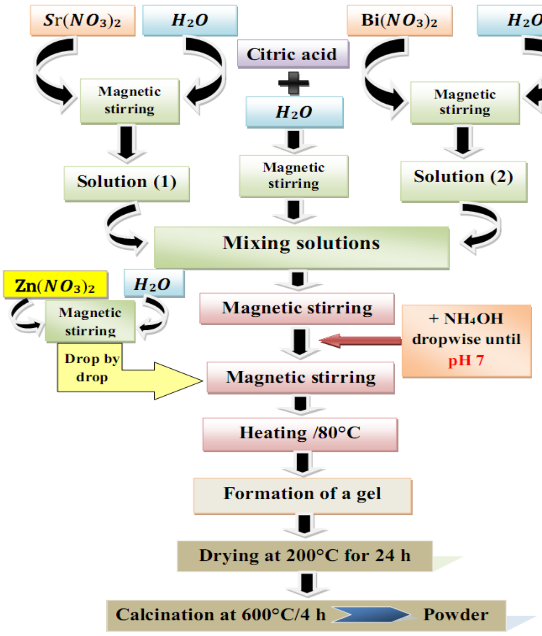

Figure 1. Diagram of the synthesis protocol of pure and Zn-doped $SrBi_2O_4$ by sol-gel process.

- *Materials characterization.* X-ray diffraction (XRD) was used for the structural studies of the undoped and zinc-doped $SrBi_2O_4$ nanoparticles using Rigaku Miniflex 600 diffractometer through CuKα radiation (0.154056 nm). The data were collected within the range of 0°–80° with a step size of 0.02°. The surface morphology of the nano-particles was studied by scanning electron microscopy (SEM) images using a Tescan Bruker model. Fourier transform infrared spectroscopy analysis has been performed on a Shimadzu FTIR-8400 spectrometer using KBr pellet technique in the range of 4000–400 cm^{-1}. ASAP 2420 multi-sampler volumetric device was used to determine nitrogen adsorption–desorption isotherms of the powder samples.

- *Photocatalytic experiments.* The tests of materials' photocatalytic activities were performed by the degradation of Congo red ($300 \leq \lambda \leq 550$ nm) under visible light irradiation in a laboratory-mounted device (Fig. 2). The visible light source used was a white lamp LED of 12 Watt (1.4 10^5 lm/m^2) positioned perpendicularly above the suspension at a distance of 8 cm. Briefly, 0.5 g of the as-synthesized photocatalysts was dispersed in 500 mL of aqueous CR solution (7 mg/L) with pH of the suspension (~6.0) at room temperature. Before lighting the lamp, the mixture was stirred in the dark for 30 min to properly disperse the photocatalyst nanoparticles and ensure adsorption-dissociation equilibrium. During the reaction, volumes were withdrawn from the solution at regular time intervals, filtered and then analyzed by UV-Vis spectrophotometry.

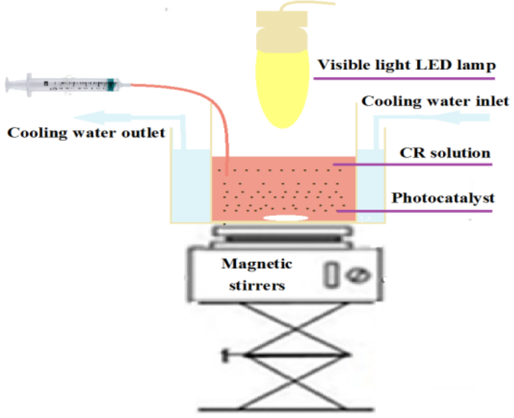

Figure 2. Schematic diagram of the photocatalytic device.

RESULTS AND DISCUSSION

Characterization

X-ray diffraction is a non-destructive characterization technique that does not damage the crystal structure of the solid sample. It allows understanding of atomic and molecular arrangements and identification of crystalline phases in the sample. X-ray diffraction spectra of the prepared samples were collected using a Rigaku miniflex 600 X-ray diffractometer with a Cu-Kα line (λ=1.5406 Å). The measurement was started after the analysis conditions such as scanning speed (2°/min) and 2θ interval (0°-80°) were set on the instrument. The diffractograms presented in Figure 3 clearly show the presence of reflections (211), (220), (002), (310), (112), (202), (411), (420), (213) and (332) belonging to $SrBi_2O_4$ [13]. Some peaks indexed to the monoclinic phase of Bi_2O_3 were identified. Additionally, low-intensity reflections related to the crystalline phase of zinc oxide were observed in the doped samples.

The crystallographic properties of the phase formed in the prepared samples were estimated from the most intense peak at 2θ = 27.50°. The Debye-Scherrer equation was used to estimate crystallite size as follows [14]:

$$D = \frac{0{,}9\lambda}{\beta \mathrm{Cos}(\theta)} \qquad (1)$$

where λ is the wavelength of the radiation used in Cu Kα (0.15406 nm), β is the full width at half maximum (in rad) of the peak and θ is the angle at the position of the maximum peak (in rad).

Microstrain was calculated by the Williamson-Hall method [15]:

$$\varepsilon = \frac{\beta}{4tan\theta} \qquad (2)$$

The dislocation density is affected by the change in the average crystallite size and consequently by the doping rate. The relationship between the average crystallite size and the dislocation density is expressed by the equation:

$$\delta = \frac{1}{D^2} \qquad (3)$$

The results of the calculations of the average crystallite size (D), microstress (ε) and dislocation density (δ) are grouped in Table 1. The values thus obtained indicate that the particle size of $SrBi_2O_4$ decreases with increasing Zn concentration. This shows that the nanoparticles of the doped samples are less agglomerated than those of the undoped sample. The microstrain values increase with increasing Zn content due to the effect of the nanoparticle size on the overall stress of the materials. The number of dislocation lines per unit area inside the materials increases with decreasing crystallite size [16].

Table 1. Average grain size (D), mean microstrain (ε) and dislocation density (δ) of the photocatalysts.

	SB	SBZ (1%)	SBZ (3%)	SBZ (5%)
D (nm)	43.24	28.52	27.43	27.44
ε	0.00337	0.00514	0.00533	0.00531
δ	0.000534	0.00122	0.00132	0.00132

The FTIR spectra of the prepared samples (Fig. 4) show that (i) these samples have a spinel structure through the appearance of two main characteristic absorption bands around 507 cm^{-1} and 435 cm^{-1} according to the Waldron hypothesis [17]. The vibrations of the tetrahedral stretching were recorded at a higher wavenumber than those of the octahedral stretching, because the A-O bond in the tetrahedral site is shorter than the B-O bond in the octahedral site [18]. (ii) Zinc substitution caused an increase in the intensity of the absorption peak at 507 cm^{-1} which can be attributed to an incorporation of zinc ions into the tetrahedral site (preferred site of Zn^{2+} ions). The FTIR spectra of all doped samples exhibit the same characteristic peaks as that of the undoped oxide, illustrating the similar nature of the chemical bonds. The interaction between the incorporated zinc ions and the native strontium ions can be inferred from the change in intensity of the FTIR spectra and the slight shift of the peaks to either side, depending on the doping level corresponding to the M-O bond [19]. Finally, the band at about 1435 cm^{-1} in the undoped spectrum corresponds to the absorption characteristics of carbonate ions (CO_3^{2-}) on the sample surface [20].

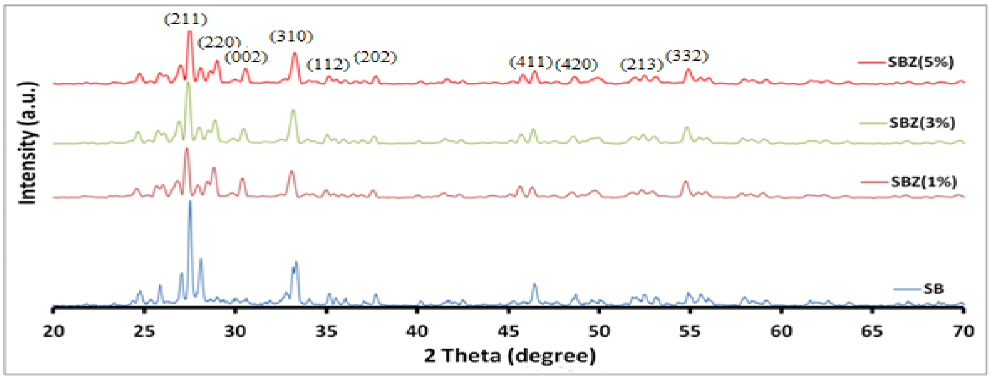

Figure 3. XRD patterns of pure and Zn-doped $SrBi_2O_4$ nanoparticles.

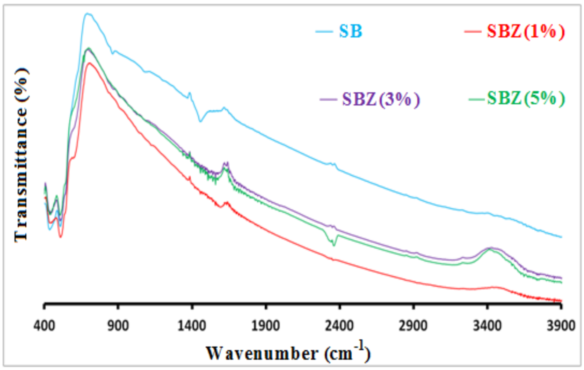

Figure 4. FTIR spectra of the photocatalysts.

The SEM study, whose micrographs are shown in Figure 5, was carried out on pure and Zn-doped $SrBi_2O_4$. The microstructures show an irregular distribution of agglomerated grains throughout the samples. Apparently, the particle size gradually decreases with increasing dopant concentration.

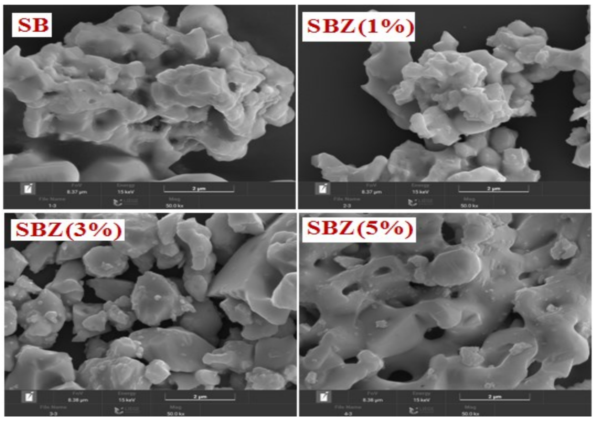

Figure 5. SEM micrographs of pure and doped $SrBi_2O_4$.

The Brunauer-Emmett-Teller (BET) adsorption-desorption isotherms for pure $SrBi_2O_4$ and Zn-doped $SrBi_2O_4$ samples synthesized through the sol–gel method are displayed in Figure 6. The textural properties of the synthesized samples are depicted in Table 2. The isotherms shown in Figure 6 are almost of the same shape and can be classified as type III according to the Brunauer-Deming-Deming-Teller (BDDT) classification, typical of macroporous materials [21, 22]. All powders display very low specific surfaces between 0.1429 and 0.3549 m² g^{-1}. These results are in excellent agreement with the value cited by Shtarev *et al.* (0.13 m² g^{-1}) [9]. According to calculations using the Barrett-Joyner-Halenda (BJH) method (Table 2), the synthesized photocatalysts have pore volume ranging from 8.2 12^{-4} cc/g to 12.8 10^{-4} cc/g and size ranging from 12.58 nm to 22.70 nm.

Table 2. Textural properties of pure and Zn-doped $SrBi_2O_4$.

	SB	SBZ (1%)	SBZ (3%)	SBZ (5%)
Surface area (m^2/g)	0.3549	0.1429	0.2508	0.3173
Pore size (nm)	12.58	17.68	16.28	22.70
Pore volume (cm³/g)	0.00121	0.00082	0.00097	0.00128

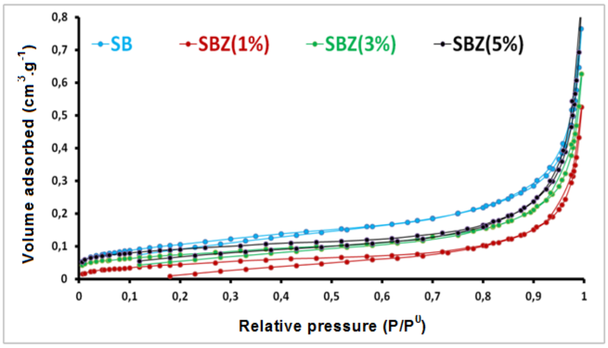

Figure 6. BET analysis of the fabricated photocatalysts.

- *Photocatalytic activity.* Both undoped and zinc-doped materials showed promising photocatalytic degradation of Congo red dye. This degradation was found to be a function of the reaction time as shown in Figure 7, where the initial strong absorption peak visible around 498 nm gradually decreased with time. However, in the case of 3% doped $SrBi_2O_4$, the CR degradation was 84% within 180 min of irradiation, which was comparatively better. The effect of Zn doping on the photocatalytic activity of the $SrBi_2O_4$ system can be explained by the ability of the Zn^{2+} ion to combine with hydroxyl ions to form the coordination ion $[Zn(OH)_4]^{2-}$, which further increases the hydroxyl content on the surface of the photocatalyst and consequently increases the amount of adsorbed dye [23]. Furthermore, at a doping concentration of 3%, impurity energy levels form within the band gap of $SrBi_2O_4$, leading to its narrowing and consequently increased light absorption. Simultaneously, the zinc dopant ions create shallow potential wells that trap electrons, thus promoting the separation of photogenerated electron-hole pairs and minimizing their recombination [24]. When the Zn^{2+} doping concentration increases (5%), the Fermi level shifts into the conduction band, resulting in a significant increase in the band gap due to the Burstein-Moss effect and, consequently, a decrease in visible light absorption [25]. In addition, excess zinc acts as a recombination center and covers the active sites on the surface of $SrBi_2O_4$, thus reducing the efficiency of charge separation [26].

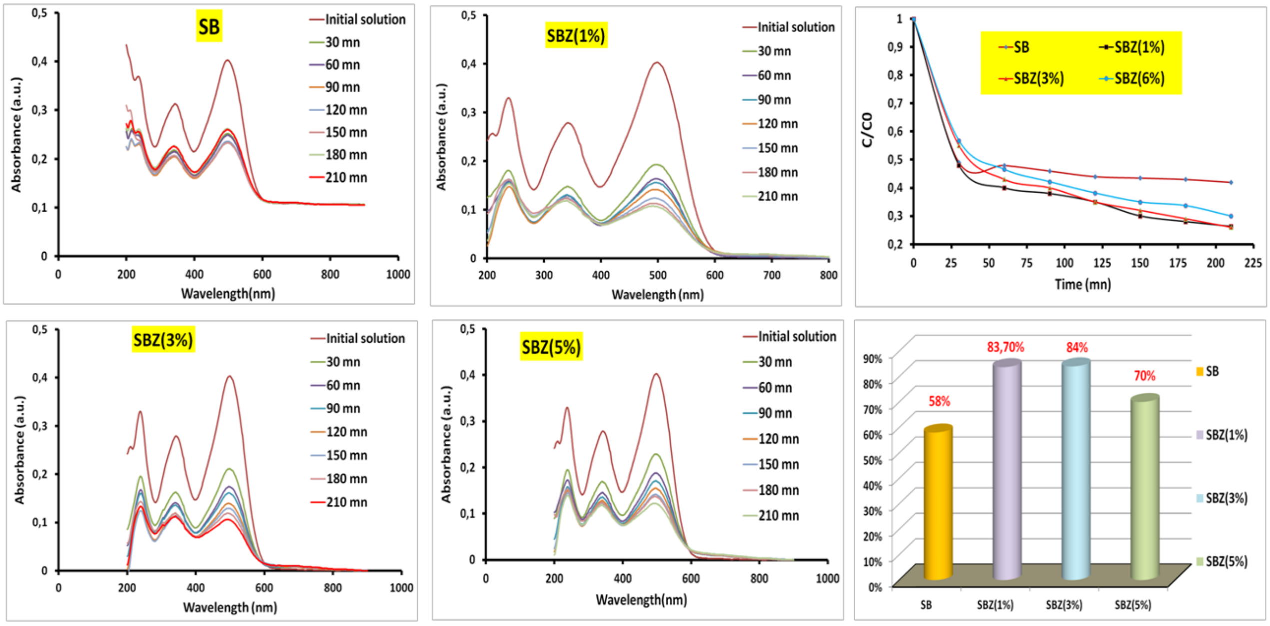

Figure 7. Degradation of CR dye: intensity change with irradiation time, C/C_0 *vs.* time plot.

Table 3. Comparison of the photocatalytic performance of Zn-doped $SrBi_2O_4$ under visible light (this work) with some photocatalysts reported in the literature.

S. no	Catalyst material	Pollutant	Time (min)	Degradation (%)	Ref.
1	Zn-doped NiO	Congo red	120	57	[30]
2	Zn-dopedTiO_2	Methylene blue	120	92.6	[31]
4	Zn-doped Nb_2O_5	Rhodamine B	180	90	[32]
5	Zn/Al-TiO_2	Congo red	120	81.24	[33]
6	$Zn_xCd_{0.8-x}Mn_{0.2}Al_{0.1}Fe_{1.9}O_4$	Congo red	80	93.12	[34]
7	$TiO_2.[ZnFe_2O_4]_{0.1}$	Congo red	300	90	[35]
8	Ag-$CuBi_2O_4$	Rhodamine B	60	91.7	[36]
9	$NaNbO_3/CuBi_2O_4$	Rhodamine B	90	75	[37]
10	$ZnO/NiBi_2O_4$	Malachite green	120	92.30	[38]
11	$Zn/SrBi_2O_4$	Congo red	210	84	This work

Few studies have examined the photocatalytic activity of $SrBi_2O_4$ under visible irradiation; however, spinel bismuth-based photocatalysts such as $ZnBi_2O_4$, $CuBi_2O_4$ and $NiBi_2O_4$ have been the subject of several studies. Telmani *et al.* (2019) reported that the total degradation of methylene blue (30 mg/L) at neutral pH was achieved in less than 2 h on a $NiBi_2O_4/ZnO$ heterojunction [27]. Nafees *et al.* (2022) obtained an ammonia removal rate of 96% using a $CuBi_2O_4$/PANI composite [28]. Nguyen *et al.* (2020) proposed the use of a hybrid photocatalyst (rGO/$ZnBi_2O_4$). Applied to the photodegradation of 2,4-dichlorophenoxyacetic acid, the catalyst showed better catalytic performance with more than 90% degradation [29].

The photocatalytic activity of the present photocatalysts under visible light was compared with that of some photocatalytic systems reported, and the results are presented in Table 3.

- *Kinetic analysis.* A simplified Langmuir–Hinshelwood (L–H) kinetic model (equation 4) was used to describe the photocatalytic degradation rate of CR by plotting the graph of $-\ln(C/C_0)$ *versus* time, t, (Figure 8(a)) [39].

$$-ln\frac{C}{C_0} = k_{app}t \qquad (4)$$

where C_0 and C are the concentrations of Congo red in solution at time 0 and t, respectively, and k_{app} is the apparent first-order reaction rate constant.

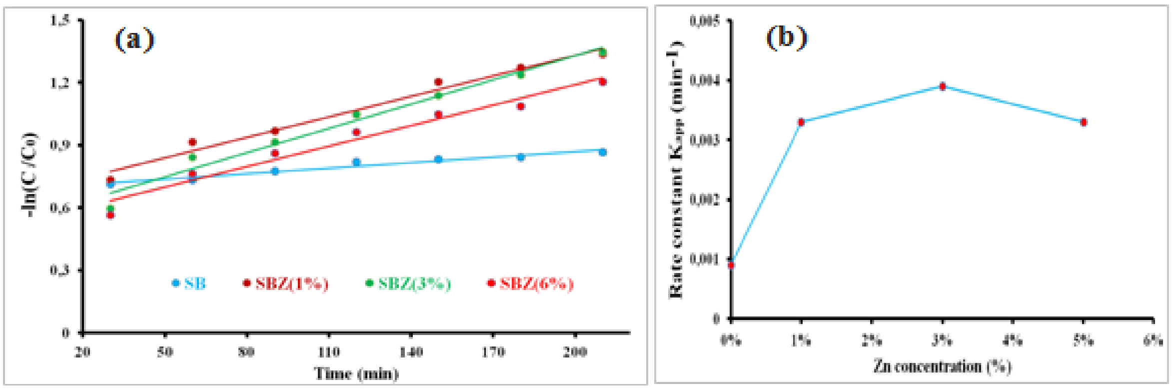

Figure 8. Pseudo-first-order kinetic curves (a) and reaction rate constant (k_{app}) (b) of the degradation of CR at diferent Zn contents.

The slopes of the curves, obtained by plotting $-\ln(C/C_0)$ as a function of time, were used to determine the rate constants (K_{app}) of the different photocatalysts. The graphical representation of the rate constants as a function of the Zn doping level (Fig. 8(b)) clearly confirms the effect of zinc doping on the photocatalytic activity of $SrBi_2O_4$. The highest degradation rate of Congo red was achieved at 3% Zn. The energy diagram and the suggested mechanism of the photocatalytic degradation of Congo red under visible light illumination are illustrated in Figure 9 and Eqs. (5) to (9):

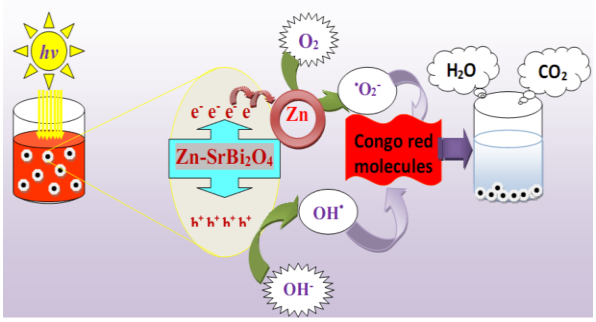

Figure 9. Schematic illustration of the photocatalytic degradation process of Congo red dye onto SBZ photocatalyst.

$$SrBi_2O_4 + hv \rightarrow SrBi_2O_4(e^-_{CB} + e^-_{VB}) \quad (5)$$

$$\begin{cases} e^-_{CB} + Zn^{2+} \rightarrow Zn^{1+} \\ Zn^{1+} + O_2 \rightarrow Zn^{2+} + O_2^{-\bullet} \end{cases} \quad (6)$$

$$e^-_{CB} + O_2 \rightarrow O_2^{-\bullet} \quad (7)$$

$$\begin{cases} h^+_{VB} + OH^- \rightarrow HO^\bullet \\ h^+_{VB} + H_2O \rightarrow H^+ + HO^\bullet \end{cases} \quad (8)$$

$$\begin{cases} O_2^{-\bullet} \\ HO^\bullet \end{cases} + CR \rightarrow \textit{degradation products}\ (CO_2 + H_2O + \bullet\bullet\bullet\bullet) \quad (9)$$

CONCLUSIONS

In this study, the photocatalytic degradation reaction of Congo red, one of the water pollutants, was carried out in the presence of pure and doped spinel photocatalysts. For this purpose, pure and zinc-doped $SrBi_2O_4$ catalysts at 1, 3 and 5% were prepared by sol-gel method. In the photocatalytic degradation reactions of Congo red under visible radiation, half-hour dark time, initial CR concentration of 7 mg/L, and catalyst amount of 1 g/L were considered as optimal reaction conditions, and all prepared catalysts were tested under these conditions.

A kinetic study of the reaction was carried out. The formation of spinel crystalline phases was confirmed by X-ray diffraction and infrared spectroscopy. Crystallographic calculations revealed a reduction in the average crystallite size and an increase in microstress and dislocation density with the increase in doping rate. All materials displayed a relatively good photocatalytic activity towards the Congo red dye with a clear superiority of the photocatalysts doped at 1 and 3% which gave degradation rates of 83.7 and 84%, respectively. These results showed the possibility to further improve the photocatalytic activity of the spinel $SrBi_2O_4$ (i) by optimizing the preparation conditions and the photocatalytic process (pH in particular) and (ii) by considering other dopants.

Acknowledgement: *We thank the Ministry of Higher Education and Scientific Research of Algeria for the financial assistance allocated to the research. The authors thank the Platform CARPORVISU from the University of Liège for the nitrogen adsorption-desorption measurements. S. D. Lambert thanks the "Fonds National de la Recherche Scientifique" for her position as Research Director. The authors thank the "Région Wallonne" for its financial contribution.*

REFERENCES

1. M. M. S. Mahbubul, Md H. Shakhawat, Md K. Rajaul, Fa U. Mohammad, H. Mahady, H K. Razib, *Environ. Sustain. Indic.,* **18,** 100247 (2023).
2. V.P. Dinesh, P. Biji, A. Anuradha, S.K. Dhara, M. A. Kamaruddin, K. Tyagi, R. Baldev, *RSC Adv.,* **4**, 58930 (2014).
3. M.D. Murcia, M. Gómez. E. Gómez, J.L. Gómez, N. Christofi, *Desalination,* **281**, 364 (2011).
4. E. Akbar, N. Simin, Y. Bahram, M. Alireza, V. Foroogh, N, Ramin, N. Shahrokh, *J. Chem. Technol. Biotechnol,* .**83**,1447 (2008).
5. W. Fei, Y. Hua, Z. Yunchuan, *Mater. Sci. Semicond. Process.,* **73**, 58 (2018).
6. H J. Zaid, H G. Bassim, H A. Saad, G. Athraa, A M. Taher, A M. Abrar, *Solar Energy*, **282**(1), 112988 (2024).
7. H.A. Enayatullah, S. Raja, A. Adeel, P. Junqing, *Colloids Surf. A: Physicochem. Eng. Asp.,* **684**, 1331855 (2024).
8. C. O. Olalekan, S. Lawrence, L Y. Tunde, C. O. Damian, *J. Water Process. Eng.,* **66**, 105890 (2024).
9. D.S. Shtarev, N. Serpone, *J. Photochem. Photobiol. C: Photochem*., **50**, 100501 (2022).
10. Z. Shan, Y. Xia, Y. Yang, H. Ding, *F. Mater. Lett.* **63**, 75 (2009).
11. X. Hu, C. Hu, J. Qu, *Appl. Catal., B Environ*., **69**, 17 (2006).
12. C. Hu, X. Hu, J. Guo, J. Qu, *Environ. Sci. Technol.*, **40**, 5508 (2006).
13. S. Rezaei, A. Gholizadeh, D. Kalhor, *J. Sol-Gel Sci. Technol.,* **115**, 1336 (2025).
14. B.D. Cullity, S.R. Stock, Elements of X-Ray Diffraction, Prentice Hall, 2001.
15. P. Rajeswari, S. Dhanuskodi, *Cryst. Res. Technol.,* **48**, 589 (2013).
16. E F. Abo Zeid, I A. Ibrahem, M A. Atif, A. A. M. Walied, *Results Phys.*, **12**, 562 (2019).
17. W. Qin, T. Nagase, Y. Umakoshi, J. A. Szpunar, *J. Phys. Condens. Matter.,* **19**, 236217 (2007).
18. D. Yu, Y. Yifu, S. Huixia, *Electrochim. Acta,* **56**, 9433 (2011).
19. A.N. Naveen, S. Selladurai, *Electrochim. Acta,* **125**, 404 (2014).
20. S. S. N. Clament, K. R. Thinesh, K. L. John, V J. Judith, *J. Alloys Compd.,* **509** (41), 9809 (2011).
21. H. Mittal, A. Al Alili, S. M. Alhassan, *Micropor. Mesopor. Mat.* **299**,110106 (2020).
22. H. Li, J. Lin, J. Wu, J. Wang, P. Wang, G. Kang, S. Huang, M. Fu, J. Wei, Z. Ding, J. Long, *Adv. Sci*, **12**, 2412082(2025).
23. X. Zhong-Lian, W. Xuan-Yi, T. He-Yun, P. Aprea, H. Shi-You, *Chin. J. Inorg. Chem.,* **37**, 1700 (2021).
24. Y. Chen, Z. Liu, Y. Yan, L. Liu., *Inorg. Chem. Commun*., **180**, 115123 (2025).
25. C.G. Jin, T. Yu, Z.F. Wu, F. Wang, M.Z. Wu, Y.Y. Wang, Y.M. Yu, L.J. Zhuge, X.M. Wu, *Appl. Phys. A.,* **106**, 961 (2012).
26. Y. Chen, Z. Liu, Y. Yan, L. Liu., *Inorg. Chem. Commun*., **180**, 115123 (2025).
27. K. Telmani, H. Lahmar, M. Benamira, L. Messaadia, M. Trari, *Optik,* **207**, 163762 (2020).
28. A. Nafees, A. Jerry, K. Zain, S. Suhail, C. Pablo, C. Frederic, *Heliyon,* **8**, e10210 (2022).
29. M T. Nguyen, N K. Dang, Q T. Nguyen, L. Yong, T K P. Nguyen, *Environ. Sci. Pollut. Res*., **27**, 11127 (2020).
30. M. Keerthana, M. Ingle, T. Pushpa Malini, R. Sangavi, *Rasayan. J. Chem*., **15**,1646 (2022).
31. Y. Zou, T. Yu, X. Huang, Y. Li, L. Guo, H. Yan, J. Zhou, Y. Wang, *Mater. Res. Express*, **10**, 085005 (2023).
32. J. A. Oliveira, M. O. Reis, M. S. Pires, L.A.M. Ruotolo, T.C. Ramalho, C.R. Oliveira, L.C.T. Lacerda, F.G.E. Nogueira, *Mater. Phys. Chem*., **228**,160 (2019).
33. N. Yuliasari, A. Amri, R. Mohadi, E. Elfita, A. Lesbani, *Sci. Technol. Indones*.,**7**, 449 (2022).
34. M. Yasar, M. Ibrahim, M. Zeeshan, K. Javed, F. Noreen, *React. Kinet. Mech. Catal.,* **137**, 2807 (2024).
35. H. Narayan, H. Alem, *Int. J. Nanosci. Nanotechnol.,* **13**, 315 (2017).
36. F. Wang, H. Yang, Y. Zhang. *Mater. Sci. Semicond. Process.,* **73**, 58 (2018).
37. K. D. Rajan, P.P. Gotipamul, S. Khanna, S. Chidambaram, M. Rathinam, *Mater. Lett*., **296**, 12990 (2021).
38. T. C. Esnawan, D. O. B. Apriandanu, R. M. Surya, H. Watarai, M. Ridwan, Y. Yulizar, *Mater. Lett.,* **365**, 136387 (2024).
39. Z. Z. Vasiljevic, M. P. Dojcinovic, J. D. Vujancevic, I. Jankovic-Castvan, M. Ognjanovic, N. B. Tadic, S. Stojadinovic, G. O. Brankovic, M. V. Nikolic, *R. Soc. Open Sci.,* **7**, 200708 (2020).